

Featuring research from Soft & Smart Materials & Devices (SSMD) Laboratory, Korea Advanced Institute of Science and Technology (KAIST), Republic of Korea.

An immunosensor based on a high performance dual-gate oxide semiconductor thin-film transistor for rapid detection of SARS-CoV-2

Immunosensor for detecting SARS-CoV-2 was based on high performance dual-gate (DG) oxide semiconductor thin-film transistor (TFT). This immunosensor could rapidly and accurately measure the electrical changes originated from SARS-CoV-2. This study demonstrates the potential of DG oxide semiconductor TFT-based immunosensors as SARS-CoV-2 sensing platforms.

As featured in:



See Sehun Jeong et al.,
Lab Chip, 2022, **22**, 899.



Cite this: *Lab Chip*, 2022, **22**, 899

An immunosensor based on a high performance dual-gate oxide semiconductor thin-film transistor for rapid detection of SARS-CoV-2[†]

Jingyu Kim, ‡^a Sehun Jeong, ‡^a Siracosit Sarawut, ^a Haneul Kim, ^b Seong Uk Son, ^{cd} Seungheon Lee, ^b Gulam Rabbani, ^b Hyunhwa Kwon, ^b Eun-Kyung Lim, ^{cd} Saeyoung Nate Ahn^{be} and Sang-Hee Ko Park ^{*a}

Severe acute respiratory syndrome coronavirus 2 (SARS-CoV-2) is the agent of an infectious disease that has led the WHO to declare its highest level (6) pandemic. The coronavirus disease 2019 (COVID-19) has spread rapidly around the world, and the number of confirmed cases has passed 246 million as of November 2021. Therefore, precise and fast virus detection protocols need to be developed to cope with the rapid spread of the virus. Here, we present a high performance dual-gate oxide semiconductor thin-film transistor (TFT)-based immunosensor for detecting SARS-CoV-2. The immunosensor has an indium tin oxide sensing membrane to which the antibody against the SARS-CoV-2 spike S1 protein can be immobilized through functionalization. The dual-gate TFT was stable under ambient conditions with near-zero hysteresis; capacitive coupling yields a 10.14 ± 0.14 -fold amplification of the surface charge potential on the sensing membrane and improves the pH sensitivity to 770.1 ± 37.74 mV pH⁻¹ above the Nernst limit. The immunosensor could rapidly detect the SARS-CoV-2 spike S1 protein and cultured SARS-CoV-2 in 0.01× PBS with high antigen selectivity and sensitivity. Our immunosensor can accurately measure the electrical changes originated from SARS-CoV-2, without the need for polymerase chain reaction tests or labeling.

Received 11th December 2021,
Accepted 7th February 2022

DOI: 10.1039/d1lc01116b

rsc.li/loc

Introduction

Unknown pneumonia cases, later named severe acute respiratory syndrome coronavirus 2 (SARS-CoV-2), were reported on December 31, 2019, by the WHO China Country Office.¹ The common symptoms were fever, cough, myalgia, and fatigue.² Clinical specimens received from patients in

various countries were inconsistent with previously known respiratory pathogens such as MERS-CoV and SARS-CoV.² Recent studies have revealed that SARS-CoV-2 can be transmitted among humans and infects cells by binding to the angiotensin-converting enzyme 2 acting as a cellular entry receptor.^{3,4} On March 12, 2020, the WHO declared the highest level (6) pandemic to respond to the rapid spread of the infection.⁵ As of November 2, 2021, approximately 2 years after the first report, more than 246 million infections and over 5 million deaths have been recorded.⁶

To respond to the pandemic, development of various diagnostic methods is essential. The most common diagnostic method is the reverse transcription-polymerase chain reaction (RT-PCR), which involves the amplification of the amount of DNA and the reverse transcription from viral RNA into DNA.⁷ Measurements by monitoring the amount of specific viral RNA, however, take 1.5 to 4 h depending on the equipment.⁷ Hence, various technologies for rapid diagnostics have been developed. Representative examples are paper-based electrochemical biosensors, field-effect transistor (FET) based biosensors, SARS-CoV-2 HC-FIA-based lateral flow immunoassay (LFIA), and cellular entry receptor-based LFIA.^{8–11}

Oxide semiconductors are promising candidates for materials of the active channel layer of thin-film transistors

^a Department of Materials Science and Engineering, Korea Advanced Institute of Science and Technology (KAIST), 291 Daehak-ro, Yuseong-gu, Daejeon, 34141, Republic of Korea. E-mail: shkp@kaist.ac.kr

^b Nano Diagnostics & Devices (NDD), Room B-312 IT, Medical Fusion Center, Gumiidae-ro, 350-27, Gumi-si, Gyeongbuk, 39253, Republic of Korea

^c BioNanotechnology Research Center, Korea Research Institute of Bioscience and Biotechnology (KRIBB), 125 Gwahak-ro, Yuseong-gu, Daejeon, 34141, Republic of Korea

^d Department of Nanobiotechnology, KRIBB School of Biotechnology, University of Science and Technology (UST), 217 Gajeong-ro, Yuseong-gu, Daejeon, 34113, Republic of Korea

^e Fuzbien Technology Institute, 12111 Parklawn Drive, Lab 130, Rockville, MD 20852, USA

[†] Electronic supplementary information (ESI) available: Antibody immobilization, electrical operation, output curve, contact angle images, XPS, storage stability, and real time detection of SARS-CoV-1 spike S1 protein. See DOI: 10.1039/d1lc01116b

[‡] These authors have contributed equally to this work.

(TFTs) owing to their ultra-low leakage current, high electron mobility, excellent electrical stability, scalability, and easy processing.^{12,13} Owing to their excellent electrical properties, oxide semiconductors are being actively developed not only for switching and driving transistors, but also as sensing materials in gas detectors and phototransistors for sensor applications.^{14–16} In addition, TFTs with dual-gate (DG) structures can detect pH, biochemicals, and pressure by means of signal amplification through the capacitive coupling with the sensing region isolated from the TFT device.^{17–20} Therefore, DG oxide semiconductor TFTs can be applied as immunosensors with outstanding electrical properties and high sensitivity.

Herein, we present the possibility of rapid detection of SARS-CoV-2 using an immunosensor based on DG oxide semiconductor TFTs. The electrical signal change originated from the surface charge potential on the sensing membrane is amplified by a factor of 10 according to the device operation properties. An antibody against SARS-CoV-2 was immobilized on the sensing membrane through APTES functionalization, and the antibody only binds with the SARS-CoV-2 spike S1 protein by antibody–antigen selective interaction, as identified from the analysis. The limit of detection (LOD) of the immunosensor was 2.30 fg mL⁻¹ for the SARS-CoV-2 spike S1 protein, and the immunosensor

rapidly detected the antigen in a wide detection range with high sensitivity, as demonstrated by real-time detection. Furthermore, through reaction comparisons with the MERS-CoV spike S1 protein, the antigen selectivity of the immunosensor was verified. In addition, our immunosensor successfully detected cultured SARS-CoV-2 in real-time detection.

Materials and methods

Device fabrication

A schematic illustration of the fabrication process is shown in Fig. 1a. A 150 nm-thick layer of ITO-coated glass was used as a sensing membrane as well as the bottom gate electrode of the DG oxide semiconductor TFT. A 30 nm-thick layer of Al₂O₃ bottom gate insulator was deposited by plasma-enhanced atomic layer deposition at 300 °C. Then, a 20 nm-thick Al doped ITZO active channel layer was deposited by RF-sputtering. The channel width and length were 80 and 20 μm, respectively. Pre-annealing was performed under oxygen conditions at 350 °C for 2 h. After pre-annealing, an 80 nm-thick Mo source and drain (S/D) electrodes were formed by DC-sputtering. A 200 nm-thick layer of SiO₂ top gate insulator was deposited by plasma-enhanced chemical vapor deposition at 300 °C, and the Mo top gate (80 nm-thick) was

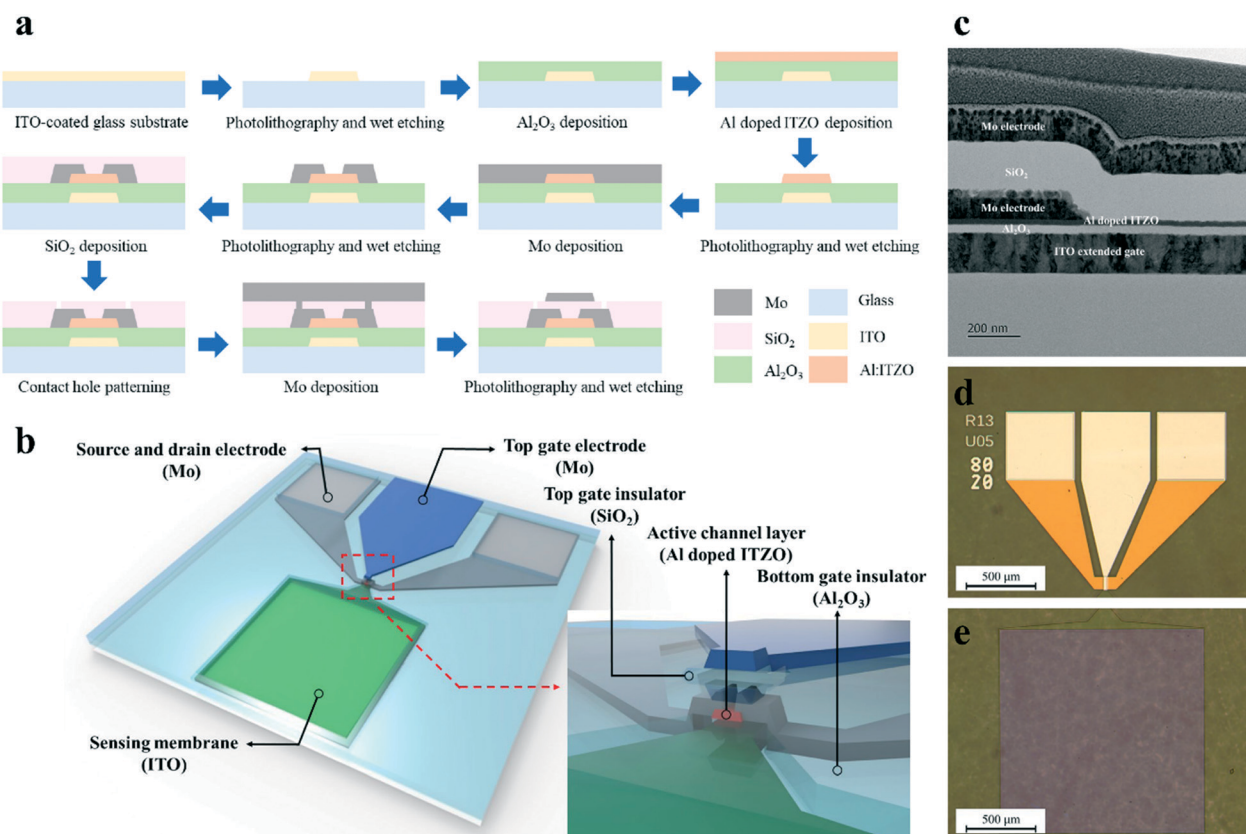


Fig. 1 Schematic illustration of the fabrication process and images of the dual-gate thin-film transistor. Schematic illustration of (a) the fabrication process and (b) the dual-gate thin-film transistor. (c) TEM image of the dual-gate thin-film transistor (cross-sectional view). Optical microscope images of (d) the operating part and (e) the sensing part in the dual-gate thin-film transistor (top view).

deposited by DC-sputtering. Photolithography and wet etching were employed to design the gate electrodes, active channel layer, contact hole, and S/D electrodes. Fig. 1b shows a schematic illustration of the device. The cross-sectional and top view images of the DG TFTs were obtained by transmission electron microscopy (JEM-2100F, JEOL LTD) and optical microscopy, shown in Fig. 1c–e. The fabricated DG TFTs were post-annealed in a vacuum at 325 °C for 2 h. Finally, the PET reservoir was attached to the ITO sensing membrane to prevent overflow of the biochemical solution.

Immobilization of SARS-CoV-2 antibody

A schematic illustration of the immobilization process is shown in Fig. S1.† To increase the number of hydroxyl groups on the surface of the ITO sensing membrane, a UV-ozone treatment (AC-6, AHTECH LTS) was performed on the DG TFTs for 20 min. The DG TFTs were then soaked in 5 wt% APTES (Sigma Aldrich) in ethanol for 1 h under ambient conditions and annealed at 150 °C for 10 min in a vacuum oven. Subsequently, the ITO sensing membrane was treated with MES buffer solution mixed with a crosslinker of 20 mM EDC (Sigma Aldrich) and 50 mM NHS (Sigma Aldrich) for 1 h under ambient conditions to improve the reactivity with the carboxyl group. After functionalization, the sensing membrane was treated with 100 µg mL⁻¹ SARS-CoV-2 spike S1 antibody (cat: 40150-R007, Sino Biological) in 0.01× phosphate-buffered saline (PBS). Finally, the blocking procedure was performed with 1 wt% BSA (Sigma Aldrich, USA) in 0.01× PBS for 20 min under ambient conditions. After each step, the DG TFTs were rinsed with ethanol and DI water several times.

Surface characterization

The contact angle and wetting energy were evaluated by using a contact angle analyzer (Phoenix-300, SEO). X-ray photoelectron spectroscopy (K-alpha, Thermo VG Scientific) was used to confirm the elemental composition and chemical bonding state with an Al K α X-ray source. The scanned X-ray photoelectron spectroscopy (XPS) spectra were charge-shifted based on the Ar 2p peak at 241.9 eV. SEM (JSM-7610F, JEOL) analysis was performed to visually confirm the antibody–antigen interaction and antigen selectivity. The samples for SEM were prepared by dropping 0.01× PBS (volume: 1 µL) including only AuNPs, AuNPs conjugated with the SARS-CoV-2 spike S1 protein, and the MERS-CoV spike S1 protein onto the antibody immobilized sensing membrane, respectively, and rinsed with DI water several times.

Real-time detection of spike proteins and SARS-CoV-2

Real-time detection of the SARS-CoV-2 spike S1 protein (cat: 40591-V08H, Sino Biological) in 0.01× PBS was performed at various lower spike protein concentrations (1 fg mL⁻¹, 10 fg mL⁻¹, 100 fg mL⁻¹, and 1 pg mL⁻¹) and higher concentrations (1 pg mL⁻¹, 10 pg mL⁻¹, 100 pg mL⁻¹, and 1 ng mL⁻¹). The spike proteins in 0.01× PBS were dropped on the sensing

membrane with a constant volume of 0.5 µL at regular intervals. To verify the antigen selectivity of the immunosensor, we performed real-time detection of the spike S1 protein of SARS-CoV-1 (cat: 40150-V08B1, Sino Biological) and MERS-CoV (cat: 40069-V08H, Sino Biological). In addition, cultured SARS-CoV-2 (inactivated with Triton-X 100 0.05%, from KRIBB) and cultured B/Brisbane/60/2008 (influenza B, from KRIBB) in 0.01× PBS were used for real-time detection.

Electrical characterization and simulation

The electrical characteristics of all the DG TFTs were measured by using an HP4156A semiconductor parameter analyzer. The operation scheme for the *I*–*V* measurement of the DG TFTs is shown in Fig. S2.† When a bottom gate bias was applied to the solution, an Ag/AgCl electrode (LF-1-100, Innovative Instruments) was used as a probe tip. To theoretically confirm the capacitive coupling of the DG TFTs, Atlas/Silvaco was used to simulate the operation of the DG TFTs. In real-time detection, the top gate bias and drain-source bias were fixed at ground potential and 0.1 V, respectively. Standard buffer solutions (Daejung Chemicals & Metals) with different pH values (3, 5, 7, and 9) were used to confirm their pH sensing characteristics. The normalized responses of the immunosensors were calculated by dividing the variation in the drain current by the initial drain current as $[\Delta I/I_0] = (I - I_0)/I_0$, where *I* and *I*₀ are the real-time drain current and the initial drain current, respectively.

Results and discussion

Electrical performance and pH sensing characteristics of the DG TFTs

Fig. 2a shows the transfer *I*–*V* characteristics of the DG TFTs by sweeping the top gate bias (*V*_g) while maintaining the bottom gate bias (*V*_{bg}) and drain-source bias (*V*_{ds}) at ground potential and 0.1 V, respectively. The inset in Fig. 2a shows the magnified forward and reverse sweeps within the subthreshold region, which indicate that the hysteresis of the transfer curve between the forward and reverse sweeps is almost negligible. These results suggest that the DG TFTs facilitate the precise detection of the immunosensor without being affected by hysteresis. The electrical properties of the DG TFTs were evaluated and are summarized in Table 1. The DG TFTs had field-effect mobilities of $44.7 \pm 0.24 \text{ cm}^2 \text{ V}^{-1} \text{ s}^{-1}$, subthreshold swings (SS) of $0.657 \pm 0.0024 \text{ V dec}^{-1}$, a turn-on voltage (*V*_{on}) of $-1.22 \pm 0.06 \text{ V}$, and an on-off current ratio (*I*_{on}/*I*_{off}) over 10^7 . The output curve of the DG TFT demonstrates that the hard saturation of the drain current occurs at *V*_{ds} below 1 V (Fig. S3†). In addition, a positive bias stress of 1 MV cm⁻¹ was applied for 3600 s to confirm the electrical reliability of the DG TFTs (Fig. 2b). *V*_{on} shifted positively by 0.039 V under positive bias stress conditions after 3600 s, which proved that the DG TFTs had high stability under ambient conditions. The high stability of the DG TFTs seems to result from the defect passivation by the

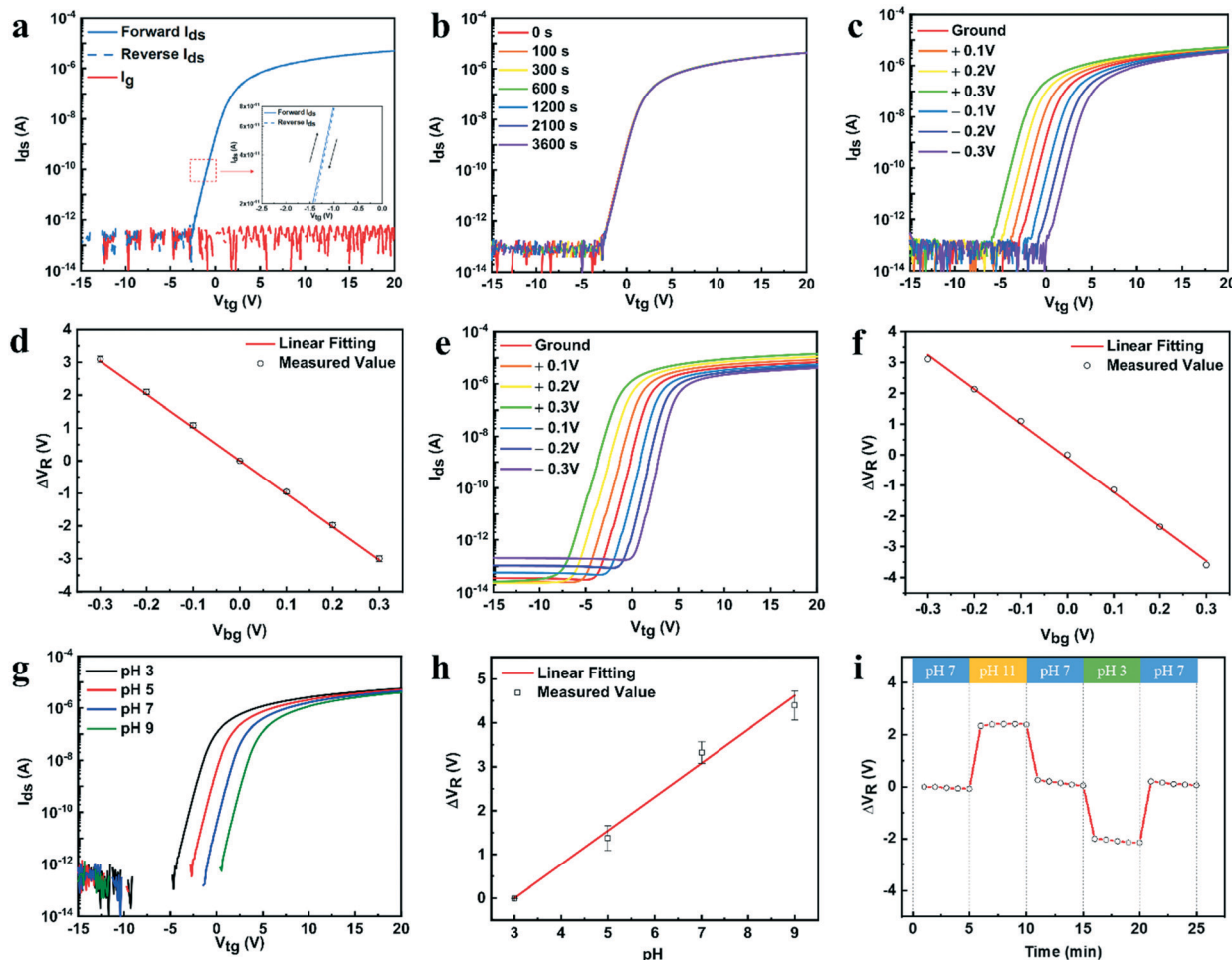


Fig. 2 Electrical properties and pH sensing characteristics of the dual-gate thin-film transistor. (a) Transfer characteristics of the dual-gate thin-film transistor ($V_{ds} = 0.1$ V). (b) Transfer curves under a positive bias stress of 1 MV cm^{-1} for 3600 s. (c) Transfer curves ($V_{ds} = 0.1$ V) and (d) reference voltage variation of the dual-gate thin-film transistor with a -0.3 V to 0.3 V range of constant bottom gate voltage at 0.1 V intervals. (e) Transfer curve ($V_{ds} = 0.1$ V) and (f) reference voltage variation with a -0.3 V to 0.3 V range of constant bottom gate voltage at 0.1 V intervals, simulated by Atlas/Silvaco. (g) Transfer curve ($V_{ds} = 0.1$ V) and (h) reference voltage variation of the dual-gate thin-film transistor in buffer solution at pH 3, pH 5, pH 7 and pH 9. (i) Measurement for the hysteresis of the reference voltage while changing pH values (pH: 7 → 11 → 7 → 3 → 7, 1 min intervals).

hydrogen supply from the Al_2O_3 or SiO_2 layers to the interface between insulators and the active channel layer during post-annealing.¹²

Fig. 2c shows the shift of the transfer curves for the DG TFTs under constant V_{bg} ranging from -0.3 V to 0.3 V at 0.1 V intervals to determine the amplification of the electrical potential. It can be seen that applying a higher V_{bg} value shifts the transfer curves toward the negative direction. Fig. 2d shows the reference voltage variation (ΔV_R) corresponding to 100 pA in the transfer curves as a function of V_{bg} . The gradient of ΔV_R was 10.14 ± 0.14 , and its R^2 was

0.9995. According to the transfer curves based on the device simulator (Atlas/Silvaco) of the equally designed DG TFTs, the constant V_{bg} increase yields the shift of the transfer curves in the negative direction as shown in the experimental results (as shown in Fig. 2e).²¹ The simulated gradient of ΔV_R was 11.18, and its R^2 was 0.9982, which is in good agreement with the experimental results (Fig. 2f). Therefore, the capacitive coupling of the DG TFTs is well established to allow the precise measurement of the electrical change, originated from the generation of surface charge potential on the sensing membrane.

To clarify the electrical changes by surface charge potential, the transfer I - V characteristics were measured while dropping the buffer solutions (volume: $2 \mu\text{L}$) with different pH values on the ITO sensing membrane (Fig. 2g). It can be seen that as the pH decreased from 9 to 3, the transfer curves shifted in the negative direction. Fig. 2h indicates that the DG TFTs have a sensitivity of 770.1 ± 37.74

Table 1 Electrical characteristics (field-effect mobility, subthreshold swing and V_{on}) of the dual gate thin film transistor

Mobility ($\text{cm}^2 \text{ V}^{-1} \text{ s}^{-1}$)	SS (V dec^{-1})	V_{on} (V)	I_{on}/I_{off}
44.7 ± 0.24	0.657 ± 0.0024	-1.22 ± 0.06	$>10^7$

mV pH⁻¹ with an R^2 value of 0.9952. This means that a pH sensitivity above the Nernst limit (59 mV pH⁻¹) was ensured and the surface charge potential applied to the DG TFTs could be amplified.²² In addition, to inspect the hysteresis caused by the reaction rate of ions near the sensing membrane, the reference voltage was measured while changing the pH values (pH: 7 → 11 → 7 → 3 → 7, 1 min intervals), as shown in Fig. 2i. The reference voltage difference between the first and last times shows a small hysteresis of 60 mV. These results confirm the high electrical reliability of the DG TFT as an immunosensor in a weakly acidic or alkaline solution, because the transfer $I-V$ characteristics do not show abnormal features such as hump generation, SS change or large hysteresis in a wide pH range. Therefore, well designed DG TFTs are appropriate for operating bio-protocols like precise immunosensors.

Characterization of bio-functionalization

APTES, which is used as a linker for the antibody, can react with a hydroxyl group through a silanization reaction and bind to the surface of the ITO sensing membrane.^{23,24} Therefore, a UV-ozone treatment was performed to increase the number of hydroxyl groups on the ITO sensing membrane for additional APTES functionalization.^{25,26} Contact angle measurements were performed to check the hydrophilicity of the ITO sensing membrane before and after the UV-ozone treatment (Fig. S4†). After the UV-ozone treatment, increased wetting energy yielded a decreased contact angle, indicating that the UV-ozone treatment

increased the hydrophilicity and generated hydroxyl groups on the ITO sensing membrane (Fig. 3a). Furthermore, the integral intensity ratio of the hydroxyl groups (531.9 eV, -OH) increased from 17.00% to 22.56% in the O 1s XPS after the UV-ozone treatment (Fig. S5†). These results indicate that the UV-ozone treatment can increase the amount of hydroxyl groups on the ITO sensing membrane.

The XPS analysis of N 1s and Si 2p was performed before and after the APTES functionalization on the ITO sensing membrane (Fig. 3b and c). After the APTES functionalization, clear peaks (red line) were observed in the N 1s (398.3 eV) and Si 2p (101.1 eV) spectra. These results show that APTES is effectively linked to the ITO sensing membrane through functionalization.

To confirm the binding affinity of the SARS-CoV-2 spike S1 protein to the antibody, scanning electron microscopy (SEM) images were acquired after dropping the 0.01× PBS containing AuNPs conjugated with the SARS-CoV-2 spike S1 protein to the antibody-immobilized ITO sensing membrane (Fig. 3e). The presence of AuNPs in the SEM image indicates that the antigen successfully bound to the antibody.²⁷ In addition, to verify the antigen selectivity of the antibody, two types of solutions containing AuNPs only and AuNPs conjugated with the MERS-CoV spike S1 protein was dropped onto the antibody-immobilized ITO sensing membrane, respectively (Fig. 3d and f). In these cases, AuNPs are not visible in the SEM images, indicating that antibody–antigen interactions did not occur.²⁷ The results demonstrated that the antibody selectively binds to the SARS-CoV-2 spike S1 protein.

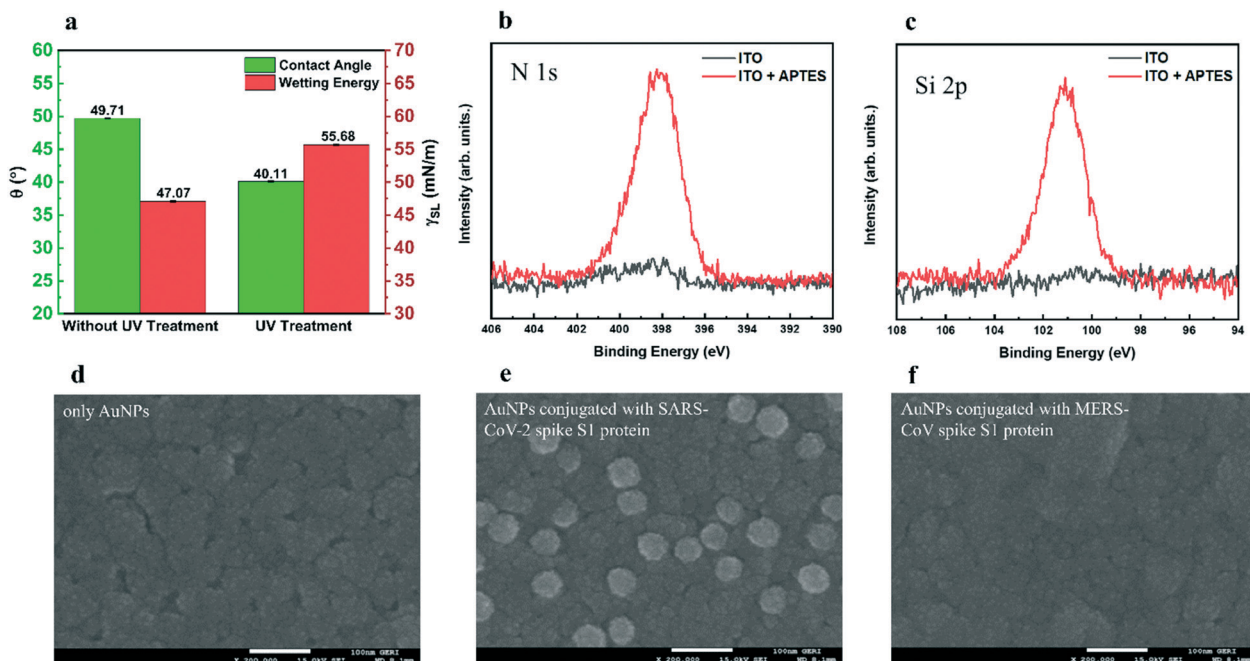


Fig. 3 Characterization of the ITO sensing membrane and antibody functionalization. (a) Contact angle and wetting energy of the ITO sensing membrane with and without UV-ozone treatment. (b) N 1s peaks and (c) Si 2p peaks from the XPS results of the ITO sensing membrane before (gray) and after (red) APTES functionalization. SEM images of the antibody immobilized ITO sensing membrane after dropping (d) only AuNPs and AuNPs conjugated with the (e) SARS-CoV-2 spike S1 protein and (f) MERS-CoV spike S1 protein in 0.01× PBS.

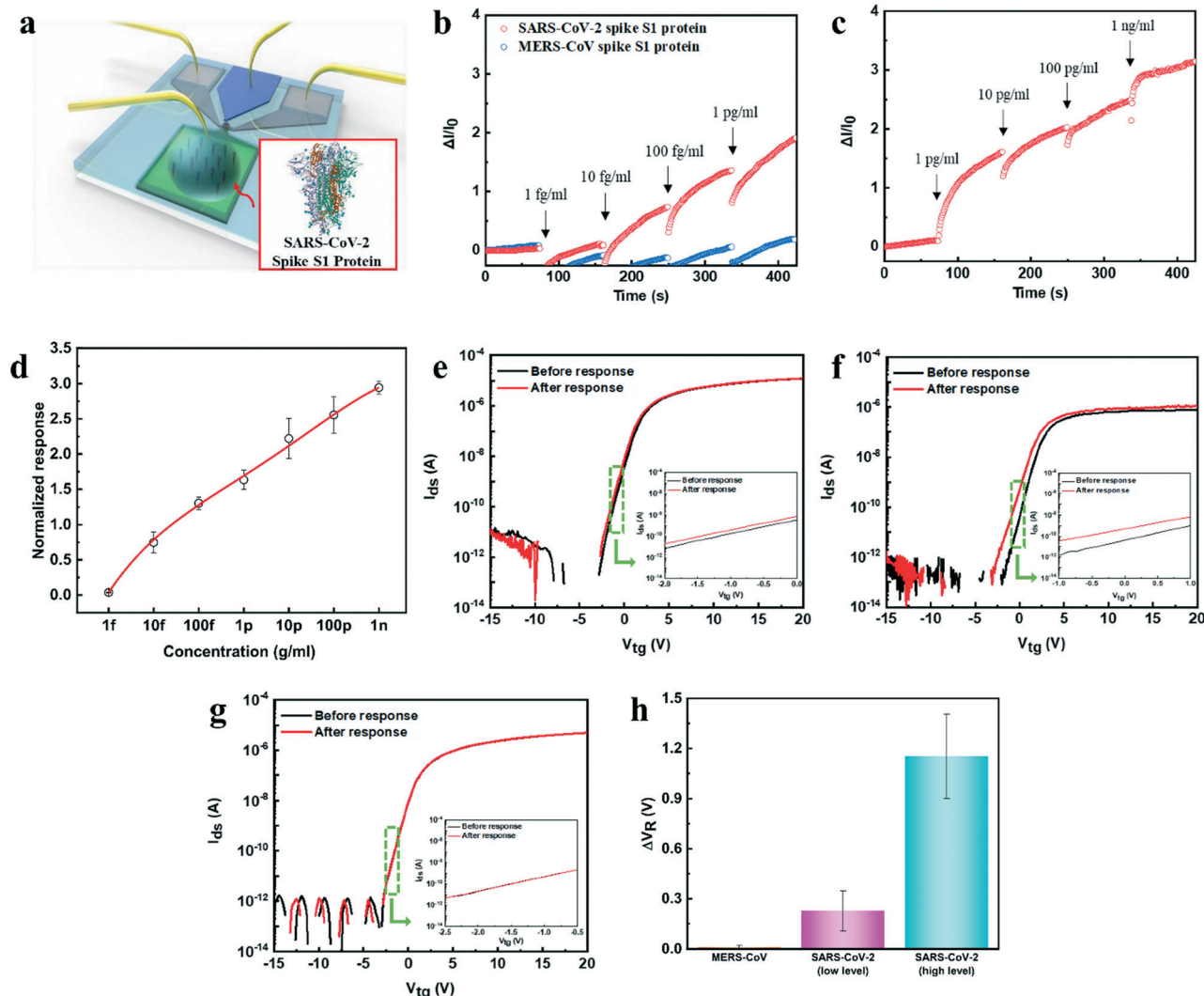


Fig. 4 Real-time detection of the SARS-CoV-2 spike S1 protein. (a) Schematic illustration of operating real time detection of the SARS-CoV-2 spike S1 protein using a dual-gate thin-film transistor-based immunosensor.²⁸ (b) Variations of the drain current during the real-time detection of the spike S1 protein of SARS-CoV-2 (red) and MERS-CoV (blue) with increasing concentration for the low level: 1 fg mL^{-1} , 10 fg mL^{-1} , 100 fg mL^{-1} and 1 pg mL^{-1} . (c) Variations of the drain current during the real time detection of the spike S1 protein of SARS-CoV-2 with increasing concentration for the high level: 1 pg mL^{-1} , 10 pg mL^{-1} , 100 pg mL^{-1} and 1 ng mL^{-1} . (d) Calibration plot for the normalized response in real-time detection of the SARS-CoV-2 spike S1 protein. Transfer curves ($V_{ds} = 0.1 \text{ V}$) of the TFTs before (black) and after (red) the response to the spike S1 protein of SARS-CoV-2 with a (e) low and (f) high level concentration range and (g) MERS-CoV. (h) Reference voltage variation of the immunosensor after the response to the spike S1 protein of SARS-CoV-2 (with a low and high level concentration range) and MERS-CoV.

Real-time detection of the SARS-CoV-2 spike S1 protein and SARS-CoV-2

Fig. 4a shows a schematic diagram of the DG TFT-based immunosensor for detecting the SARS-CoV-2 spike S1 protein. In the immunosensor, the surface charge potential generated by the interaction between the antigen and antibody is transduced into an electrical signal.¹⁸ Real-time detection of the SARS-CoV-2 spike S1 protein was performed by measuring the changes in the drain current over time with two increasing concentration series, a low level from 1 fg mL^{-1} to 1 pg mL^{-1} and a high level from 1 pg mL^{-1} to 1 ng mL^{-1} (Fig. 4b and c). As the concentration of the SARS-CoV-2 spike S1 protein in $0.01\times$ PBS increased, the response of the

drain current for the immunosensor changed noticeably in both cases. In addition, the immunosensor stored at 20°C could maintain the normalized response for over a week, indicating that the activity of the antibody was stable at room temperature for a week (Fig. S6†).

Fig. 4d shows a calibration plot for the normalized response, which was calculated from the response of the drain current 60 s after dropping the spike protein solution for each concentration in real-time detection (number of experiments: 7). The immunosensor not only had an LOD of 2.30 fg mL^{-1} , but even showed an extremely high normalized response of over 60% in all concentrations except 1 fg mL^{-1} . The characteristics of recently reported FET-based biosensors for detecting the SARS-CoV-2 spike protein are summarized

Table 2 Comparison of the performance (limit of detection, detection range, and normalized response) of previously reported FET-based biosensors for detecting the SARS-CoV-2 spike protein

Types of biosensor	LOD	Detection range	Normalized response ($\Delta I/I_0$)	Ref.
Graphene-FET	1 fg mL ⁻¹	1 fg mL ⁻¹ to 10 pg mL ⁻¹	~7% to 1 pg mL ⁻¹	9
CNT-FET	4.12 fg mL ⁻¹	0.1 fg mL ⁻¹ to 5.0 pg mL ⁻¹	~4% to 1 pg mL ⁻¹	29
CNT-FET	0.55 fg mL ⁻¹	0.55 fg mL ⁻¹ to 55 µg mL ⁻¹	~125% to 5.5 pg mL ⁻¹	30
MXene-graphene-FET	1 fg mL ⁻¹	1 fg mL ⁻¹ to 10 pg mL ⁻¹	~24% to 10 pg mL ⁻¹	31
WSe ₂ -FET	25 fg µL ⁻¹	25 fg µL ⁻¹ to 10 ng µL ⁻¹	~10% to 1.66 pg µL ⁻¹	32
Dual-gate oxide semiconductor-FET	1.17 fg mL ⁻¹	1 fg mL ⁻¹ to 1 ng mL ⁻¹	163 ± 13.6% to 1 pg mL ⁻¹	Our work

in Table 2. Compared with other FET-based biosensors, the immunosensor in this study shows a high normalized response and a prominent LOD and detection range.

Real-time detection of the MERS-CoV spike S1 protein was performed to determine the antigen selectivity for the antibody (Fig. 4b). The electrical response to different concentrations of the MERS-CoV spike S1 protein was almost negligible. Similar results were obtained for the detection of the SARS-CoV-1 spike S1 protein (Fig. S7†). These results indicate that the immunosensor has high selectivity for the antigens.

The transfer *I-V* characteristics were measured before and after the real-time detection of the spike proteins to confirm the electrical changes originated from the surface charge potential on the ITO sensing membrane (Fig. 4e-g). While the transfer curve shifts negligibly with the MERS-CoV spike S1 protein in 0.01× PBS, it shifts in the negative direction with the SARS-CoV-2 spike S1 protein in 0.01× PBS. The shift in the negative direction results from the positive charge of the SARS-CoV-2 spike S1 protein, which has an isoelectric point of 8.27, in 0.01× PBS with a pH of 7.4.³³ From Fig. 4e-g, ΔV_R corresponding to 100 pA in the transfer curve was obtained to evaluate the electrical changes quantitatively (Fig. 4h, number of experiments: 7). Unlike in the case of the MERS-CoV spike S1 protein, ΔV_R values owing to the low and high concentrations of the SARS-CoV-2 spike S1 protein were 0.227 ± 0.120 and 1.15 ± 0.253 V, respectively. These results

support that the immunosensor can transduce the charge potential of the target antigen into an electric signal with high amplification and selectivity for the target antigen.

In addition to the spike protein, actual virus samples should be detectable for the availability of diagnosis using the immunosensor. Therefore, to further investigate the electrical response of the immunosensor to a real virus sample, real-time detection of the cultured SARS-CoV-2 was carried out (Fig. 5a). Cultured SARS-CoV-2 samples in 0.01× PBS were used in real-time detection, and the viral concentrations were 10^1 , 10^2 , 10^3 , and 10^4 TCID₅₀ mL⁻¹, respectively. Influenza B with a concentration of 10^4 TCID₅₀ mL⁻¹ was used as a control. A distinct change of the normalized response was shown for each concentration of SARS-CoV-2 (LOD: 3.86 TCID₅₀ mL⁻¹) unlike in the case of influenza B (Fig. 5b, number of experiments: 5). This result demonstrates that the immunosensor properly recognized the change in electrical signals caused by SARS-CoV-2 and suggested the possibility that the immunosensor can be applied as a diagnosis platform for detecting SARS-CoV-2. In addition, Mojsoska *et al.* reported that 1700 pfu of recombinant SARS-CoV-2 correlate with 1 pg of pure spike S1 protein in Simoa assay, based on the signal.³⁴ Our immunosensor demonstrated that 1.68×10^1 TCID₅₀ (6.72×10^3 copies) of cultured SARS-CoV-2 correlate with 1 fg of spike S1 protein, based on the LOD.³⁵ Although the correlation was made through a rough criterion considering

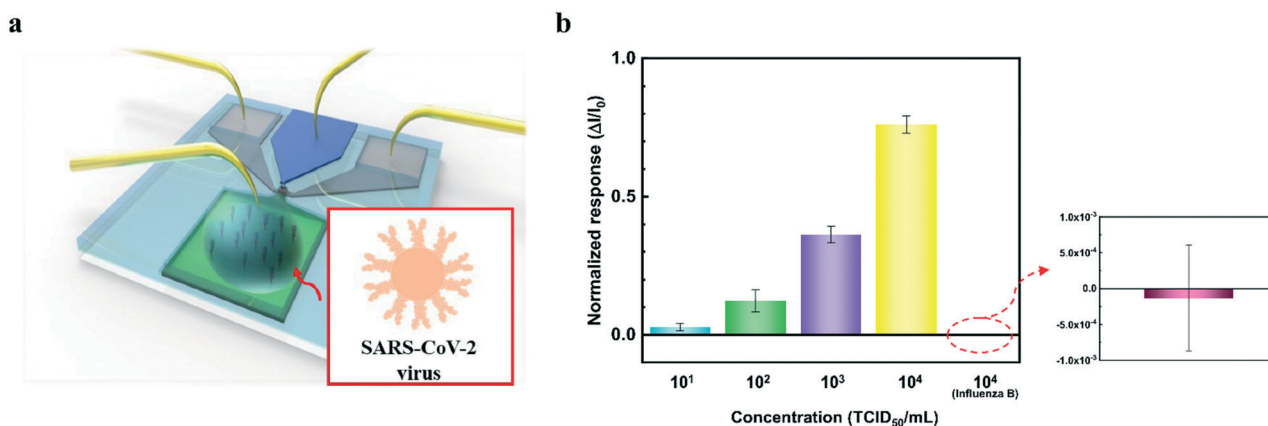


Fig. 5 Real-time detection of cultured SARS-CoV-2. (a) Schematic illustration of operating real time detection of cultured SARS-CoV-2 using the dual-gate thin-film transistor-based immunosensor. (b) Normalized response in the real-time detection of cultured SARS-CoV-2 with a concentration range from 10^1 to 10^4 TCID₅₀ mL⁻¹.

only the LOD, it is worth to estimate the detection limit in clinical samples.

Conclusions

Although various diagnostic technologies are being actively developed to overcome the COVID-19 pandemic, we presented the capability of DG TFT-based immunosensors with an antibody immobilized on the sensing membrane for detecting the SARS-CoV-2 spike S1 protein and SARS-CoV-2. The pH sensing characteristics of the DG TFT indicate that the surface charge potential on the sensing membrane is amplified through capacitive coupling in the dual-gate structure. The antibody could be immobilized on top of the ITO sensing membrane using APTES functionalization as confirmed by SEM images. The immunosensor had an LOD of 2.30 fg mL^{-1} and could rapidly detect a broad range of concentrations of the SARS-CoV-2 spike S1 protein in $0.01\times \text{PBS}$ with high electrical signal amplification and antigen selectivity in real-time detection. In addition, as in the case of detecting the SARS-CoV-2 spike S1 protein, the electrical signal caused by the cultured SARS-CoV-2 was well detected through the immunosensor. The results of this study demonstrate the potential of DG oxide semiconductor TFT-based immunosensors as SARS-CoV-2 sensing platforms which can be used for self-diagnosis tools and point-of-care testing.

Author contributions

Jingyu Kim: conceptualization, methodology, investigation, formal analysis, writing – original draft, and writing – review & editing. Sehun Jeong: software, validation, investigation, writing – original draft, and writing – review & editing. Siracosit Sarawut: software and validation. Haneul Kim: formal analysis and investigation. Seong Uk Son: investigation. Seungheon Lee: investigation. Gulam Rabbani: resources and investigation. Hyunhwa Kwon: resources. Eun-Kyung Lim: resources. Saeyoung Nate Ahn: funding acquisition and supervision. Sang-Hee Ko Park: project administration, funding acquisition, supervision, and writing – review & editing.

Conflicts of interest

There are no conflicts to declare.

Acknowledgements

This work was supported by the Alchemist project (No. 20012435) funded by the Ministry of Trade, Industry, and Energy (MOTIE, Republic of Korea).

References

- WHO, World Health Organization, Novel Coronavirus (2019-nCoV): situation report, 1, World Health Organization, 2020, vol. 205.
- P. Zhou, X. Lou Yang, X. G. Wang, B. Hu, L. Zhang, W. Zhang, H. R. Si, Y. Zhu, B. Li, C. L. Huang, H. D. Chen, J. Chen, Y. Luo, H. Guo, R. Di Jiang, M. Q. Liu, Y. Chen, X. R. Shen, X. Wang, X. S. Zheng, K. Zhao, Q. J. Chen, F. Deng, L. L. Liu, B. Yan, F. X. Zhan, Y. Y. Wang, G. F. Xiao and Z. L. Shi, *Nature*, 2020, **579**, 270.
- I. Ghinai, T. D. McPherson, J. C. Hunter, H. L. Kirking, D. Christiansen, K. Joshi, R. Rubin, S. Morales-Estrada, S. R. Black, M. Pacilli, M. J. Fricchione, R. K. Chugh, K. A. Walblay, N. S. Ahmed, W. C. Stoecker, N. F. Hasan, D. P. Burdsall, H. E. Reese, M. Wallace, C. Wang, D. Moeller, J. Korpics, S. A. Novosad, I. Benowitz, M. W. Jacobs, V. S. Dasari, M. T. Patel, J. Kauerauf, E. M. Charles, N. O. Ezike, V. Chu, C. M. Midgley, M. A. Rolfs, S. I. Gerber, X. Lu, S. Lindstrom, J. R. Verani and J. E. Layden, *Lancet*, 2020, **395**, 1137.
- J. H. Kuhn, W. Li, H. Choe and M. Farzan, *Cell. Mol. Life Sci.*, 2004, **61**, 2738.
- WHO, World Health Organization, *Coronavirus disease 2019 (COVID-19): situation report*, 52, World Health Organization, 2020, vol. 31.
- WHO, World Health Organization, *COVID-19 weekly epidemiological update*, 2 November 2021, 2021.
- A. Tahamtan and A. Ardebili, *Expert Rev. Mol. Diagn.*, 2020, **20**, 453.
- A. Yakoh, U. Pimpitak, S. Rengpipat, N. Hirankarn, O. Chailapakul and S. Chaiyo, *Biosens. Bioelectron.*, 2021, **176**, 112912.
- G. Seo, G. Lee, M. J. Kim, S. H. Baek, M. Choi, K. B. Ku, C. S. Lee, S. Jun, D. Park, H. G. Kim, S. J. Kim, J. O. Lee, B. T. Kim, E. C. Park and S. Il Kim, *ACS Nano*, 2020, **14**, 5135.
- D. Wang, S. He, X. Wang, Y. Yan, J. Liu, S. Wu, S. Liu, Y. Lei, M. Chen, L. Li, J. Zhang, L. Zhang, X. Hu, X. Zheng, J. Bai, Y. Zhang, Y. Zhang, M. Song and Y. Tang, *Nat. Biomed. Eng.*, 2020, **4**, 1150.
- J. H. Lee, M. Choi, Y. Jung, S. K. Lee, C. S. Lee, J. Kim, J. Kim, N. H. Kim, B. T. Kim and H. G. Kim, *Biosens. Bioelectron.*, 2021, **171**, 112715.
- J. B. Ko, S. H. Lee, K. W. Park and S. H. K. Park, *RSC Adv.*, 2019, **9**, 36293.
- J. H. Kim, J. Oh, K. C. Park and Y. S. Kim, *Displays*, 2018, **53**, 1.
- C. J. Chiu, S. P. Chang and S. J. Chang, *IEEE Electron Device Lett.*, 2010, **31**, 1245.
- K. S. Kim, C. H. Ahn, S. H. Jung, S. W. Cho and H. K. Cho, *ACS Appl. Mater. Interfaces*, 2018, **10**, 10185.
- H. Yoo, W. G. Kim, B. H. Kang, H. T. Kim, J. W. Park, D. H. Choi, T. S. Kim, J. H. Lim and H. J. Kim, *ACS Appl. Mater. Interfaces*, 2020, **12**, 10673.
- D. Bhatt and S. Panda, *ACS Appl. Electron. Mater.*, 2020, **2**, 2699.
- J. Lee, M. J. Kim, H. Yang, S. Kim, S. Yeom, G. Ryu, Y. Shin, O. Sul, J. K. Jeong and S. B. Lee, *IEEE Sens. J.*, 2021, **21**, 178.
- L. Liang, S. Zhang, W. Wu, L. Zhu, H. Xiao, Y. Liu, H. Zhang, K. Javaid and H. Cao, *Appl. Phys. Lett.*, 2016, **109**, 2.
- T. Yokota, T. Sekitani, T. Tokuhara, N. Take, U. Zschieschang, H. Klauk, K. Takimiya, T. C. Huang, M.

- Takamiya, T. Sakurai and T. Someya, *IEEE Trans. Electron Devices*, 2012, **59**, 3434.
- 21 Silvaco Int., *Manual, ATLAS User'S. Device simulation software*, Silvaco Int., Santa Clara, CA, 2008.
- 22 N. Kumar, J. Kumar and S. Panda, *IEEE Electron Device Lett.*, 2016, **37**, 500.
- 23 U. Hashim, S. Nadzirah, N. Azizah, M. S. Azmi and K. Bala, *Proc. - 2015 2nd Int. Conf. Biomed. Eng. ICoBE 2015*, 2015, p. 30.
- 24 M. Song, J. W. Kang, D. H. Kim, J. D. Kwon, S. G. Park, S. Nam, S. Jo, S. Y. Ryu and C. S. Kim, *Appl. Phys. Lett.*, 2013, **102**.
- 25 C. Zhang, L. Qi, Q. Chen, L. Lv, Y. Ning, Y. Hu, Y. Hou and F. Teng, *J. Mater. Chem. C*, 2014, **2**, 8715.
- 26 Z. Fan, C. Zhi, L. Wu, P. Zhang, C. Feng, L. Deng, B. Yu and L. Qian, *Coatings*, 2019, **9**, 1.
- 27 M. A. Aziz, S. Patra and H. Yang, *Chem. Commun.*, 2008, 4607.
- 28 A. C. Walls, Y. J. Park, M. A. Tortorici, A. Wall, A. T. McGuire and D. Veesler, Image from the RCSB PDB (rcsb.org) of PDB ID 6vxx, Structure, function, and antigenicity of the SARS-CoV-2 spike glycoprotein, *Cell*, 2020, **181**(2), 281–292.
- 29 M. A. Zamzami, G. Rabbani, A. Ahmad, A. A. Basalah, W. H. Al-Sabban, S. N. Ahn and H. Choudhry, *Bioelectrochemistry*, 2021, 107982.
- 30 W. Shao, M. R. Shurin, S. E. Wheeler, X. He and A. Star, *ACS Appl. Mater. Interfaces*, 2021, **13**, 10321.
- 31 Y. Li, Z. Peng, N. J. Holl, M. R. Hassan, J. M. Pappas, C. Wei, O. H. Izadi, Y. Wang, X. Dong and C. Wang, *ACS Omega*, 2021, **6**, 6643.
- 32 P. Fathi-Hafshejani, N. Azam, L. Wang, M. A. Kuroda, M. C. Hamilton, S. Hasim and M. Mahjouri-Samani, *ACS Nano*, 2021, **15**, 11461.
- 33 F. Krebs, C. Scheller, K. Grove-Heike, L. Pohl and H. Wätzig, *Electrophoresis*, 2021, **42**, 687.
- 34 B. Mojsoska, S. Larsen, D. A. Olsen, J. S. Madsen, I. Brandslund and F. A. Alatraktchi, *Sensors*, 2021, **21**, 390.
- 35 A. Amendola, G. Sberna, E. Lalle, F. Colavita, C. Castilletti, G. Menchinelli, B. Posteraro, M. Sanguinetti, G. Ippolito and L. Bordi, *J. Clin. Med.*, 2021, **10**, 1471.